

Diese Arbeit wurde vorgelegt am Aerodynamischen Institut

Investigations on two-way coupling effects of particle-laden decaying isotropic turbulent flows

PROJEKTARBEIT
VON
JULIAN STEMMERMAN, STEFFEN TRIENEKENS
UND CHRISTIAN SOIKA

Aerodynamisches Institut der RWTH Aachen

November 26, 2017

Betreuer: Konstantin Fröhlich

Erstprüfer: Univ.-Prof. Dr.-Ing. Wolfgang Schröder

Contents

I	Nomenclature	I
1	Introduction	1
2	Mathematical models	3
2.1	Equations governing the fluid phase	3
2.2	Scales of turbulent flows	4
2.3	Particle dynamics	5
3	Numerical methods	7
3.1	Discretization of the particle dynamics	7
3.2	Direct numerical simulation	8
3.3	Large-eddy simulation	8
4	Results	10
4.1	Turbulence modulation by particles	10
4.2	Simulation setup	11
4.3	Simulation results	12
5	Conclusion and outlook	16
6	References	17
7	Appendix A	19

I Nomenclature

Acronyms

DNS	Direct numerical simulation
ILES	Implicit large-eddy simulation
LES	Large-eddy simulation
PP	Particle-laden simulation
SGS	Subgrid scale
sP	Single-phase simulation

Greek Symbols

Δ	Cell length
ε	Integral dissipation rate
ε'	Additional integral particle induced dissipation rate
$\bar{\varepsilon}$	Integral dissipation rate of the flow field
γ	Isentropic exponent
η	Kolmogorov length scale
μ	Dynamic viscosity
λ_c	Ratio of physical point particles to computational point particles
ν	Kinematic viscosity
ϕ_m	Mass fraction
ϕ_v	Volume fraction
Ψ	Integral coupling rate
Ψ_p	Coupling rate for one particle
Ψ_{pp}	Integral coupling rate using the point-particle approach
ρ	Fluid density
ρ_p	Particle density
σ	Smoothing parameter
$\bar{\tau}$	Stress tensor
τ_η	Kolmogorov time scale
τ_L	Eddy turnover time
τ_p	Particle response time
ω_p	Particle angular velocity vector
Υ_f	Full fluid domain

Operators

$\frac{D}{Dt}$	Time derivative following a fluid unit
$\frac{d}{dt}$	Time derivative
δ	Small step of the following variable
$\frac{\partial}{\partial t}$	Partial derivative with respect to time

∇	Nabla operator
$:$	Inner tensor product
Roman Symbols	
A	Control surface
\mathbf{a}_p	Particle acceleration
C_d	Empirical drag coefficient
c_p	Specific isobaric heat capacity
c_v	Specific isochoric heat capacity
d_i	Distance between particle position and center of the cell
d_p	Particle diameter
E	Specific inner energy
e	Specific internal energy
E_k	Turbulent kinetic energy of the fluid
E_{kB}	Turbulent kinetic energy of the particles
\mathbf{F}	Force vector per unit volume of the particle acting on the fluid
f_D	Drag correction
\mathbf{F}_{pp}	Sum vector of forces acting on the particles
\mathbf{F}_p	Particle surface force vector
$G(r)$	Filter function
$\bar{\mathbf{H}}$	Flux tensor
$\bar{\mathbf{H}}^i$	Inviscid part of the flux tensor
$\bar{\mathbf{H}}^v$	Viscous part of the flux tensor
$\bar{\mathbf{I}}$	Identity tensor
k_t	Thermal conductivity
L	Integral length scale
Ma	Mach number
m_p	Particle mass
\mathbf{n}	Normal vector
N	Grid refinement of the simulation
N_c	Number of computational point particles
N_p	Number of physical point particles
p	Pressure
Pr	Prandtl number
\mathbf{Q}	Vector of conservative Eulerian variables
\mathbf{q}	Heat conduction vector
R	Specific gas constant
Re	Reynolds number
Re_p	Particle Reynolds number

$\bar{\mathbf{S}}$	Rate-of-strain tensor
S	Sutherland temperature
T	Temperature
t	time
t^*	Time normalized by initial eddy turnover time
\mathbf{T}_p	Particle torque vector
\mathbf{u}	Fluid velocity
U	Characteristic fluid velocity
\mathbf{u}'	Vector of fluid velocity fluctuations
\mathbf{u}_p	Vector of fluid velocity at the particle position
V	Control volume
V_p	Particle volume
\mathbf{v}_p	Particle velocity vector
v_r	Relative velocity between particle and fluid
\mathbf{x}	Position vector
\mathbf{x}_p	Particle position vector

1 Introduction

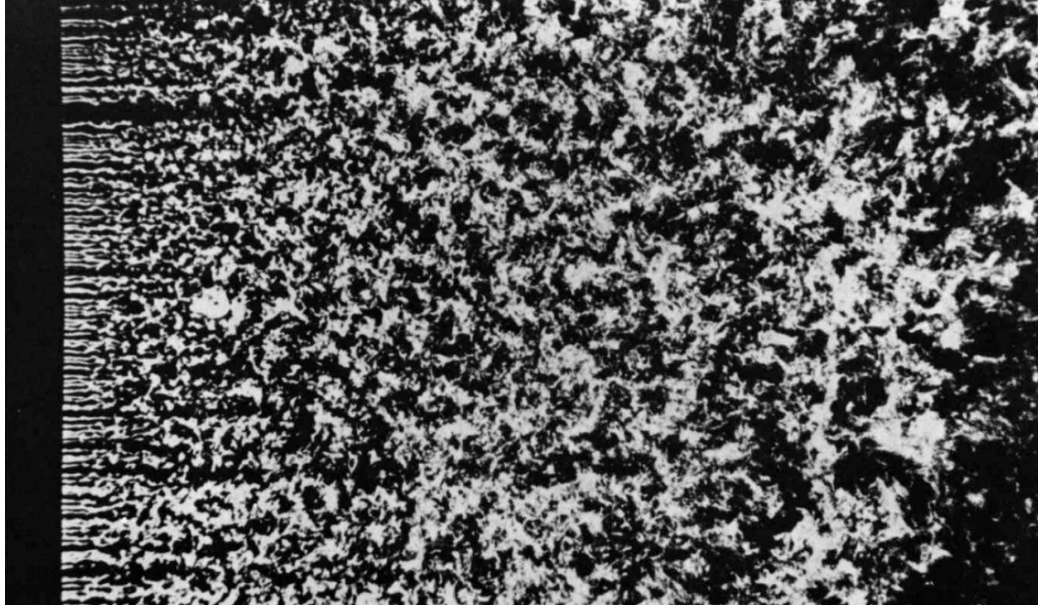


Figure 1: Photograph courtesy of Hassan Nagib and Thomas Corke. Formation of a nearly isotropic turbulent flow field behind a grid [7].

Particle-laden turbulent flows are ubiquitous in nature. Spray atomization in fuel injectors, cyclonic particle separation in oil refineries and sediment accumulation in pipelines are examples for technical applications, where it is of huge interest to predict the impact of the particles on turbulent flows. Turbulence augmentation or attenuation by particles is therefore a decisive factor.

A study about the impact of particles on the isotropic decaying turbulent flow is presented. Incompressible, isothermal and isotropic decaying turbulence will serve as the carrier flow. Gravity is omitted to avoid prominent directions. Isotropic turbulence is a relatively good assumption when a small region of a high-Reynolds-number flow, which is not affected by boundary effects, is observed [3]. This fact is visualized by Fig 1. Describing turbulent flows is a large task because of the involvement of many different scales of turbulent motion.

In this work the influence of the particles on the isotropic decaying turbulence is numerically calculated by using direct numerical (DNS) and large-eddy simulations (LES). Direct numerical simulations are able to resolve all scales of turbulent motion due to their high grid refinement. Large-eddy simulations have a lower grid resolution and use therefore a subgrid-scale model (SGS) to model these scales. This type of simulation therefore has a lower computational effort.

The simulations were carried out using the point-particle approach, where each

particle is tracked via a Lagrangian approach. The feedback of the particles on the flow field is modeled by sources and sinks, which is referred to as two-way coupling. Alternatives are one-way coupling, at which only the flow exerts influence on the particles, and four-way coupling, which extends two-way coupling by particle-particle interactions. Two-way coupling is fitting for the simulations in this study, because the volume fraction $\phi_v = 10^{-3}$ of the particles is large enough to alter the turbulence. Volume fractions below $\phi_v = 10^{-6}$ are referred to as one-way coupling and the interactions that can be observed at values greater than $\phi_v = 10^{-3}$ are called four-way coupling [14] [15]. The particle diameter is defined to be smaller than the Kolmogorov scale, i.e. the smallest scale of the turbulent flow. The particle density is much higher than the fluid density.

To lower the computational effort in general, a new variable, which describes the fraction of physical to numerical point particles, is introduced and validated.

The structure of this work is described in the following. First, mathematical models for single-phase and particle dynamics are given. Additionally, the scales of turbulent motion are described. Thereafter, the computational basics of both DNS and LES and their respective advantages and disadvantages are explained. Subsequently, the used discretization method to integrate the particle tracking equations is described and the 'computational point particles', in the following referred to as CPP, are introduced. The CPP approach is validated by analyzing turbulent kinetic energy budgets for LES and DNS. For this purpose firstly a test is conducted to find out which number of CPPs is appropriate for further evaluation. Also the number of particles that is needed to get consistent average values for the flow characteristics is investigated. Finally, a short conclusion is given.

2 Mathematical models

In this section the Navier-Stokes equations in integral formulation, the characteristic turbulent scales and the kinematic and dynamic equations for the particle phase are introduced.

2.1 Equations governing the fluid phase

The conservation of mass, momentum and energy for a control volume V reads

$$\int_V \frac{\partial \mathbf{Q}}{\partial t} dV + \int_{\partial V} \bar{\mathbf{H}} \cdot \mathbf{n} dA = \mathbf{0} \quad (2.1)$$

with time t and the flux tensor $\bar{\mathbf{H}}$. The vector \mathbf{Q} contains the variables fluid density ρ , fluid velocity \mathbf{u} and specific inner energy E :

$$\mathbf{Q} = \begin{pmatrix} \rho \\ \rho \mathbf{u} \\ \rho E \end{pmatrix}. \quad (2.2)$$

$\bar{\mathbf{H}}$ is the flux tensor which contains the inviscid and viscous flux, i.e.

$$\bar{\mathbf{H}} = \bar{\mathbf{H}}^i + \bar{\mathbf{H}}^v = \begin{pmatrix} \rho \mathbf{u} \\ \rho \mathbf{u} \mathbf{u} + p \\ \mathbf{u}(\rho E + p) \end{pmatrix} - \frac{1}{Re} \begin{pmatrix} 0 \\ \bar{\boldsymbol{\tau}} \\ \bar{\boldsymbol{\tau}} \mathbf{u} + \mathbf{q} \end{pmatrix}, \quad (2.3)$$

with the shear stress $\bar{\boldsymbol{\tau}}$, heat conduction \mathbf{q} and the pressure p . The Reynolds number $Re = \frac{\rho_\infty u_\infty l_{\text{ref}}}{\mu_\infty}$ is defined to be the ratio of inertia forces to viscous forces with reference density ρ_∞ , velocity u_∞ , length l_{ref} and dynamic viscosity μ_∞ .

The specific inner energy E and the heat conduction \mathbf{q} are defined as

$$E = e \frac{1}{2} |\mathbf{u}|^2 \text{ and} \quad (2.4)$$

$$\mathbf{q} = -\frac{\mu}{Pr(\gamma - 1)} \nabla T, \quad (2.5)$$

with the constant capacity ratio $\gamma = \frac{c_p}{c_v}$ and the Prandtl number $Pr = \frac{\mu_\infty c_p}{k_t}$ using the specific heat capacities of the fluid c_v and c_p and thermal conductivity k_t . Assuming that the fluid is newtonian, the Stokes hypothesis yields

$$\bar{\boldsymbol{\tau}} = 2\mu \bar{\mathbf{S}} - \frac{2}{3}\mu(\nabla \cdot \mathbf{u})\bar{\mathbf{I}}, \quad (2.6)$$

in which $\bar{\mathbf{S}} = \frac{(\nabla \mathbf{u})(\nabla \mathbf{u})^T}{2}$ denotes the rate-of-strain tensor. Additionally, the viscosity μ can be approximated by Sutherland's law

$$\mu(T) = \mu_\infty \left(\frac{T}{T_\infty} \right)^{3/2} \frac{T_\infty + S}{T + S}, \quad (2.7)$$

where S is the Sutherland temperature. To achieve closure the caloric state equation $e = c_v T$ and the state equation for an ideal gas $p = \rho R T$ are used. The specific gas constant is determined by $R = c_p - c_v$.

2.2 Scales of turbulent flows

Turbulent flows can be described as a superposition of chaotic, three-dimensional vortical structures of various scales (eddies). Larger eddies decay and pass their kinetic energy down to smaller scales. At the smallest scales, the kinetic energy finally dissipates into heat due to the viscous dissipation. This behavior is called the 'energy cascade' and was first described by Richardson [11] and quantified by Kolmogorov [3].

Considering homogeneous isotropic turbulence, with zero mean velocity and the integral dissipation rate ϵ , the characteristic length scales of a turbulent flow can be defined by the two-point correlation R , which is the normalized product of the velocity's fluctuation u' at two different positions \mathbf{x} and $\mathbf{x} + \mathbf{e}r$ at the same time t

$$R(r, t) = \frac{\overline{u'(\mathbf{x}, t)u'(\mathbf{x} + \mathbf{e}r, t)}}{\overline{u'^2}}, \quad (2.8)$$

as

$$\frac{1}{\lambda^2} = -\frac{1}{2} \left(\frac{\partial^2 R}{\partial r^2} \Big|_{r=0} \right), \quad (2.9)$$

$$\lambda = \sqrt{15 \frac{\nu}{\epsilon}} u' \quad (2.10)$$

or

$$L = \int_0^\infty R(r, t) dr \quad (2.11)$$

with λ being the Taylor microscale, L the integral length scale, u' denoting the absolute value of the velocity's fluctuation and \mathbf{e} pointing in the same direction as \mathbf{u}' with $|\mathbf{e}| = 1$.

The Taylor microscale can be used to compute the Taylor-scale Reynolds number

$$Re_\lambda = \frac{u' \lambda}{\nu}. \quad (2.12)$$

L and the corresponding timescale τ_L , which is most times called 'eddy turnover time', describe the large eddies. At these scales the energy is brought into the flow, creating the 'energy-containing range'. The eddy turnover time is defined by

$$\tau_L = \frac{L}{U}, \quad (2.13)$$

with the characteristic fluid velocity U .

The smallest scales in a turbulent flow are the Kolmogorov length η and time scale τ_η . At these scales, the effects of viscosity take place and the energy dissipates into heat. With the estimate $\epsilon \approx \frac{U^3}{L}$ they can be written as

$$\eta = \left(\frac{\nu^3 L}{U^3} \right)^{1/4} \quad (2.14)$$

and

$$\tau_\eta = \left(\frac{\nu L}{U^3} \right). \quad (2.15)$$

Both these scales are coupled by the Reynolds numbers

$$\frac{L}{\eta} = Re^{3/4} \quad (2.16)$$

and

$$\frac{\tau_L}{\tau_\eta} = Re_L^{1/2} \quad (2.17)$$

with $Re_L^{1/2} = \frac{u' L}{\nu}$. It can be observed from these equations that the spacing between the scales increases for higher Reynolds numbers.

2.3 Particle dynamics

\mathbf{F}_{pp} is the sum of several pressure and shear forces acting on the particles and is described explicitly by the Maxey-Riley equation [12]. Reduced to the governing forces acting on the particles and with neglect of gravity the dynamic equation of the particles becomes

$$\begin{aligned} \mathbf{F}_{pp} = m_p \frac{d\mathbf{v}_p}{dt} = \rho V_p \frac{D\mathbf{u}_p}{Dt} + 3\pi\mu d_p (\mathbf{u}_p - \mathbf{v}_p) \phi(Re_p) + \frac{1}{2}\rho V_p \left(\frac{D\mathbf{u}_p}{Dt} - \frac{d\mathbf{v}_p}{dt} \right) + \\ 3\pi\mu d_p \int_0^t K(t)(t-t') \cdot \left(\frac{d\mathbf{u}_p}{dt'} - \frac{d\mathbf{v}_p}{dt'} \right) dt'. \end{aligned} \quad (2.18)$$

$\mathbf{v}_p(\mathbf{x}_p, t)$ is the particle velocity vector with the time derivative d/dt along the particle trajectory while D/Dt is the material derivative at one point. $\mathbf{u}_p(t) = \mathbf{u}_p(\mathbf{x}_p, t)$ is the velocity of the undisturbed fluid at the particle position \mathbf{x}_p . The individual forces on the right side of the equation are stated in the following:

- $\rho V_p \frac{D\mathbf{u}}{Dt}$:
pressure gradient of the undisturbed flow
- $3\pi\mu d_p (\mathbf{u}_p - \mathbf{v}_p) \phi(Re_p)$:
quasi-steady Stokes drag that is parallel to the undisturbed streamlines and

is described by the Stokes' law as the force of viscosity acting on the interface of small spherical particles and fluid that can be achieved at very low Reynolds numbers in a viscous fluid

- $\frac{1}{2}\rho V_p \left(\frac{D\mathbf{u}}{Dt} - \frac{d\mathbf{v}_p}{dt} \right)$:
added mass force, representing the influence of the fluid's inertia that has an impact on the particle, in case of a different acceleration than the particles
- $3\pi\mu d_p \int_0^t K(t)(t-t') \cdot \left(\frac{d\mathbf{u}_p}{dt'} - \frac{d\mathbf{v}_p}{dt'} \right) dt'$:
Basset history force taking the unsteady motion into account using a history kernel $K(t)$

(2.18) is based on Stokes flow conditions, i.e., vanishing particle Reynolds number $Re_p \ll 1$. In addition in this thesis, particles with $d_p \ll \eta$ are investigated. As a result for heavy particles, the drag force is the dominating contributor of Eq. (2.18) as reported by [18]. Therefore \mathbf{F}_{pp} can be reduced to

$$\mathbf{F}_{pp} = m_p \frac{d\mathbf{v}_p}{dt} = 3\pi\mu d_p (\mathbf{u}_p - \mathbf{v}_p) \phi(Re_p). \quad (2.19)$$

$\phi(Re_p) = 1 + 0.15Re_p^{0.687}$ is an empirical correction factor for finite Re_p .
Eq. (2.19) can be reformulated to

$$\frac{d\mathbf{v}_p}{dt} = \frac{\phi(Re_p)}{\tau_p} (\mathbf{u}_p - \mathbf{v}_p), \quad (2.20)$$

with the particle relaxation time $\tau_p = \frac{1}{18} \frac{\rho_p}{\rho_f} \frac{d_p^2}{\nu}$.

Together with the kinematic equation

$$\frac{d\mathbf{x}_p}{dt} = \mathbf{v}_p, \quad (2.21)$$

the Eqs. (2.1) and (2.19) form a closed system of equations.

3 Numerical methods

Two numerical methods are discussed and their main differences pointed out in the following chapter, the DNS (direct numerical simulation) and the LES (large-eddy simulation). The basis of both are the Navier-Stokes equations as described above. The simulations were carried out using ZFS, the simulation tool developed and implemented at the Institute of Aerodynamics at RWTH Aachen University [5] [6]. The tool is capable of simulating compressible finite-volume flows using unstructured Cartesian grids.

3.1 Discretization of the particle dynamics

To compute the Lagrangian particle trajectories, a predictor-corrector scheme based on the trapezoidal rule for numerical integration

$$f(t + \delta t) \approx f(t) + \frac{\delta t}{2} \left[\frac{\partial f(t)}{\partial t} + \frac{\partial f(t + \delta t)}{\partial t} \right] \quad (3.1)$$

is used.

The first step is the prediction of the new particle position $\mathbf{x}_{p,n+1}$ using a Taylor expansion for a small time step δt

$$\mathbf{x}_{p,n+1} = \mathbf{x}_{p,n} + \delta t \mathbf{v}_{p,n} + \frac{1}{2} \delta t^2 \mathbf{a}_{p,n}, \quad (3.2)$$

with $\mathbf{a}_{p,n}$ particle acceleration, where the subscript p denotes the particle and the subscript n the time step.

To avoid filtering effects, the fluid velocity $\mathbf{u}(\mathbf{x}_{p,n+1})$ at the particle position $\mathbf{x}_{p,n+1}$ is set equal to the nearest cell fluid velocity.

The predicted velocity and acceleration are calculated with

$$\mathbf{v}_{p,n+1} = \frac{\mathbf{v}_{p,n} + \frac{1}{2} \delta t \left(\mathbf{a}_{p,n} + \frac{f_d}{\tau_p} \mathbf{u}(\mathbf{x}_{p,n+1}) \right)}{1 + \frac{1}{2} \frac{f_D}{\tau_p} \delta t}, \quad (3.3)$$

$$\mathbf{a}_{p,n+1} = \frac{\frac{f_D}{\tau_p} (\mathbf{u}(\mathbf{x}_{p,n+1}) - \mathbf{v}_{p,n}) - \frac{1}{2} \delta t \mathbf{a}_{p,n}}{1 + \frac{1}{2} \frac{f_D}{\tau_p} \delta t}. \quad (3.4)$$

The updated particle position must be corrected by an additional term according to the trapezoidal rule

$$\mathbf{x}_{p,n+1} = \mathbf{x}_{p,n} + \frac{1}{2} \delta t (\mathbf{v}_{p,n+1} + \mathbf{v}_{p,n}) + \frac{1}{12} \delta t^2 (\mathbf{a}_{p,n+1} - \mathbf{a}_{p,n}). \quad (3.5)$$

These approaches to compute the particle trajectories require a lot of computational resources. Due to reduce this requirement clusters of point particles are

created. For this purpose the ratio λ_c of physical point particles N_p to CPPs N_c is introduced ($\lambda_c = \frac{N_p}{N_c}$). To compensate this lack of particles, the feedback force is multiplied by λ_c , due to the λ_c -fold mass of the (cluster-)particles.

To model the impact of the particles on the fluid, the Navier-Stokes equations (2.1) are extended by momentum sources or sinks. The feedback force of the particles is exerted on the fluid using a distance based weighting function

$$\mathbf{F} = \mathbf{F}_{pp} \cdot \frac{e^{-(d_i^2/(\sigma\Delta^2))}}{\sum_i e^{-(d_i^2/(\sigma\Delta^2))}}, \quad (3.6)$$

with the distance between particle position and the cell center d_i , the grid width Δ , and a smoothing parameter σ that controls the distribution of \mathbf{F} on the adjacent cells.

3.2 Direct numerical simulation

With DNS, the Navier-Stokes equations are solved completely. This provides a very accurate result, as all scales of motion are being resolved. Still it requires an immense level of computational resources which increases rapidly with the Reynolds number: $N \propto Re_\lambda^{9/2}$ with the gridsize N of the simulation. With the LES, as described below, the computational effort is 99.98 % less compared to DNS, which indeed is the fraction of the dissipative scale. This leaves 0.02 % of the flow, which is correlative with the fraction of the energy-containing larger-scale [13].

3.3 Large-eddy simulation

Due to the fact that DNS is effortful, LES was created to save time and resources. The energy containing larger-scale motion is completely resolved and the small effects of the smaller-scale motion are modeled. Otherwise in DNS resolving the small dissipative scale would require most of the computational resources.

Simulating only the larger-scale motions is called filtering, which means that the smaller-scale motions, also known as fluctuation, are filtered out. The filtered velocity field is calculated by $\bar{U}(\mathbf{x}) = \int_{-\infty}^{\infty} G(\mathbf{r})U(\mathbf{x} - \mathbf{r}) d\mathbf{r}$, with $G(\mathbf{r})$ being a homogeneous filter function. For further information on filter functions, the works of Pope [13] should be considered. To model the filtered smaller-scale motions usually a subgrid-scale (SGS) model is used. According to Hickel (2007) the interference between explicit SGS and the truncation error can be exploited, i.e.

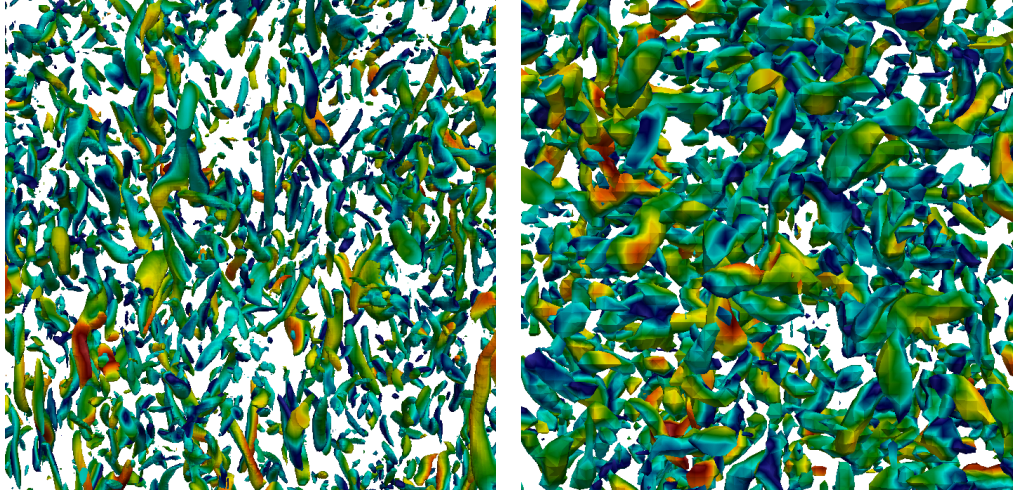


Figure 2: Comparison between DNS and LES. 'Worm-like' structures in an isotropic flow field simulated in different grid resolutions. The more refined grid on the left show more and better resolved structures, while the right picture reveals more artificially generated artifacts. For creation see Appendix A.

the truncation error can serve as model of the effects of unresolved scales, which is therefore an implicit SGS model. Thus it is called implicit LES (ILES) [16].

4 Results

In this section, the properties and results of the DNS and LES of particle-laden decaying isotropic turbulence which have been carried out will be presented. An additional test to find out which number of CPPs could be used is presented. Special emphasis will be put on the turbulent kinetic energy budgets and their use to interpret the findings.

4.1 Turbulence modulation by particles

The particle-laden turbulence modulation by particles in decaying isotropic turbulence is determined by the coupling rate Ψ , which describes the energy transfer between both fluid and particle phase, the background dissipation rate of the flow field $\bar{\epsilon}$ and the particle-induced dissipation rate ϵ' . These variables form an equation which describes the change in turbulent kinetic energy:

$$\frac{dE_k}{dt} = \Psi(t) - \bar{\epsilon}(t) - \epsilon'(t). \quad (4.1)$$

As the dissipation rate is always of positive value, it acts as a sink for the fluid's turbulent kinetic energy. In difference to that, the coupling rate can serve either as source or sink, depending on the acceleration of the particles [1]. The coupling rate for fully resolved particles Ψ is defined as

$$\Psi(t) = \sum_{p=1}^{N_p} \Psi_p = - \sum_{p=1}^{N_p} (\mathbf{F}_p \cdot \mathbf{v}_p + \mathbf{T}_p \cdot \boldsymbol{\omega}_p), \quad (4.2)$$

using surface force \mathbf{F}_p , particle velocity \mathbf{v}_p , torque \mathbf{T}_p and angular velocity $\boldsymbol{\omega}_p$ to describe the transfer of kinetic energy resulting at each particle.

As mentioned before, the flow field is considered nearly incompressible, therefore the equation for the viscous dissipation rate can be approximated by

$$\epsilon(t) \approx 2\mu \bar{\mathbf{S}} : \bar{\mathbf{S}}, \quad (4.3)$$

where $:$ denotes the inner tensor product. This rate can then be integrated over the fluid domain excluding particles and their direct surroundings Υ_f , leading to the background flow field dissipation rate

$$\bar{\epsilon}(t) = \int_{\Upsilon_f} \epsilon(t) dV. \quad (4.4)$$

Additionally the particles change the fluid's rate of dissipation due to their volume forces. The additional dissipation rate for fully resolved particles can be computed

by

$$\varepsilon' = \sum_{p=1}^{N_p} \mathbf{F}_p \cdot (\mathbf{u}_p - \mathbf{v}_p) + \mathbf{T}_p \cdot (\mathbf{\Omega}_p - \mathbf{\omega}_p), \quad \rho_p \gg \rho, \quad (4.5)$$

using the velocity of the fluid \mathbf{u}_p and the vorticity vector of the undisturbed flow about one particle $\mathbf{\Omega}_p$, both at the particle position. Fluid inertia and hydrostatic and shear stresses were neglected in this study.

For $\rho_p \gg \rho$ and the point-particle approach the coupling rate Ψ and the additional dissipation rate ε' are implicitly coupled. Torque and angular velocity were neglected for the used point-particle approach, leading to

$$\Psi_{pp}(t) = \Psi - \varepsilon'(t) = - \sum_{p=1}^{N_p} \mathbf{F}_p \cdot \mathbf{u}_p. \quad (4.6)$$

This leads to

$$\frac{dE_k}{dt} = \Psi_{pp}(t) - \bar{\varepsilon}(t) = - \sum_{p=1}^{N_p} \mathbf{F}_p \cdot \mathbf{u}_p - \bar{\varepsilon}(t). \quad (4.7)$$

4.2 Simulation setup

All cases were simulated on a cubic domain and a Cartesian grid using different grid refinement levels. For the LES-cases 64^3 , 96^3 and 128^3 are employed, hence the need to model smaller scales with SGS-models, which have already been validated in [9]. For a DNS, 256^3 cells are necessary to resolve all scales.

The particle-free case was initialized using a seed-based number random generator, a process which is described in detail in [17]. At the initial eddy turnover time $t^* = t \frac{\varepsilon_0}{u_0^3} \approx 0.27 = t_{inj}^*$, using the initial viscous dissipation rate ε_0 and initial rms-velocity u_0 , a restart file is written out to initialize the subsequent simulation of the particle-laden isotropic turbulence.

This file is then used to set up a second simulation, where the particles are initialized at random positions with the fluid velocity. The single-phase DNS and particle-laden DNS will be used as reference for analyzing other results. The single-phase results will be in the following referred to as sP, and particle-laden results as PP. The PP simulations are set up to match the volume fraction $\phi_v = \frac{V_p}{V_f} = 10^{-3}$ and mass fraction of $\phi_m = \frac{m_p}{m_f} = 1$. The density ratio was set to $\frac{\rho_p}{\rho} = 1000$ and the particle diameter is $d_p \approx 0.6\eta_0$ with η_0 being the initial Kolmogorov length. At the timestep of injection the Reynolds number at the Taylor microscale was $Re_\lambda \approx 58$.

4.3 Simulation results

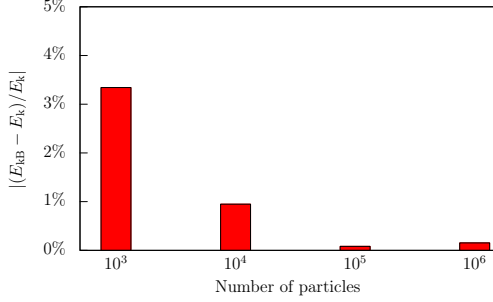


Figure 3: Initializing different numbers of point-particles for a LES_{128} . An inaccuracy can be observed for small numbers of particles. This behavior can be observed for all other resolutions. The relative deviation of turbulent kinetic energy of particles and carrier flow is below 1% for 10^4 particles.

The first set of simulation was set up to investigate how different numbers of injected particles have an influence on the difference of turbulent kinetic energy of both particle and fluid. As mathematical description of turbulent flows is based on statistics, small numbers of particles can lead to questionable results.

An example for the deviation in kinetic energy for different numbers of particles can be found in Fig. 3. The normalized difference in kinetic energy E_{kB} of the particles and the flow itself E_k shows a correlation between particle number and accuracy in this single simulation. One-time simulations in other grid sizes show similar results. This simulations served as test and a first evaluation, which number of CPPs are purposeful to simulate. As the flow statistics are relatively accurate for simulations with only 10^4 particles, the method of CPPs could be a useful tool to lower computational effort. This leads to the assumption that simulations with a λ_c of 100 seem fitting with an overall number of a million particles. The second set of simulations of this study is set up to investigate the influence of CPPs on the accuracy of the simulations to find out which amount can be implemented without high loss in accuracy. For this purpose, the variable λ_c , which was established before, was implemented in the program code. All simulations were then set up with the overall same number of a million particles, altering the CPPs. Simulations were conducted for $\lambda_c = 10, 50$ and 100 . Additionally simulations of the single-phase flow and an unclustered particle-laden flow were conducted. A DNS was serves as reference for later evaluations.

It can be seen in Fig. 4 that the decay in turbulent kinetic energy E_k normalized by initial turbulent kinetic Energy $E_{k,0}$ from the injection point depends highly on the number of clustered particles. It can be stated that the flow's statistics for high λ_c converge towards the sP-case.

As it can be seen in Fig. 5 the behavior of lower-resolution particle-laden simulations seems to be less prone to CPPs, as the lower-resolution simulations are more similar to the PP-DNS reference.

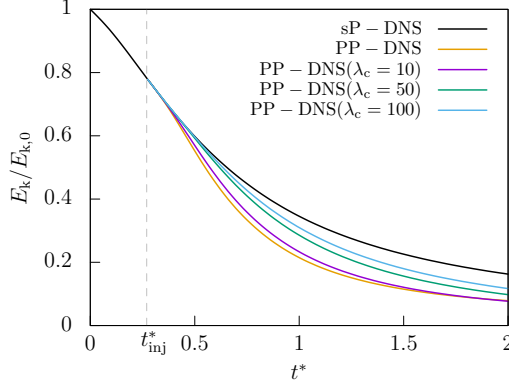


Figure 4: Kinetic energy E_k normalized by its initial value $E_{k,0}$ over time normalized by initial eddy turnover time. Shortly after the injection the PP-cases separates from the sP-flow. The higher-clustered cases show significant differences compared to the reference case PP-DNS.

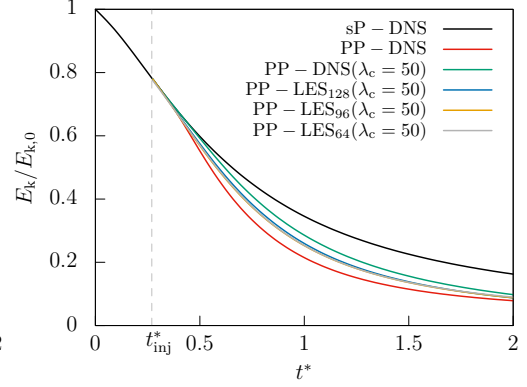


Figure 5: Kinetic energy E_k normalized by its initial value $E_{k,0}$ over time normalized by initial eddy turnover time for different grid resolutions and with constant $\lambda_c = 50$. The lower-resolution simulation results are more similar to the particle-laden reference case PP-DNS.

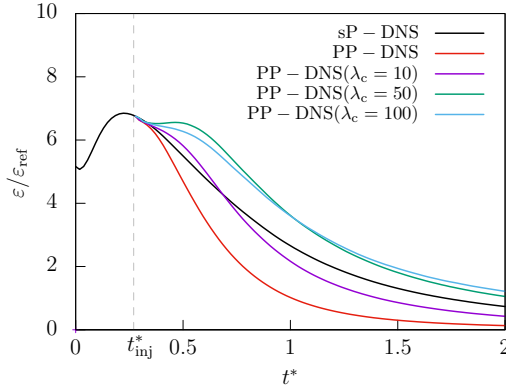


Figure 6: Normalized dissipation rate $\bar{\varepsilon}$ over time normalized by initial eddy turnover time. The unclustered PP-case shows a lower dissipation rate than the sP-case. Highly clustered PP-cases show a higher dissipation rate.

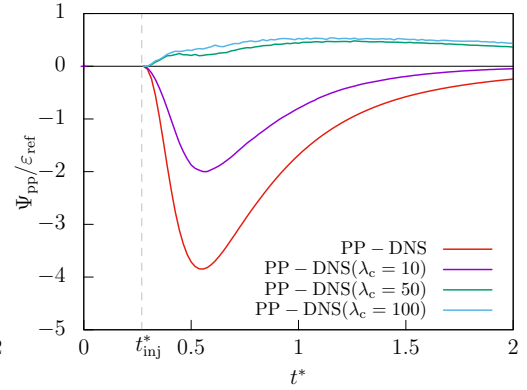


Figure 7: Normalized point-particle coupling rate Ψ_{pp} over time normalized by initial eddy turnover time. The PP-case without clustering shows the lowest coupling rate. Both highly-clustered PP-cases show physically questionable behavior.

Case	λ_c	$\frac{m_c}{m_{V, \text{cell}}}$	$\epsilon \frac{u_0^3}{L}$	$\frac{\lambda}{L}$	$\frac{\eta}{L}$	Re_λ	$E_k/E_{k,0}$	$E_{kB}/E_{k,0}$
DNS	1	16.78	0.97	0.039	0.0032	38.73	0.21	0.29
	10	167.78	2.08	0.028	0.0026	28.66	0.23	0.34
	50	838.86	3.51	0.024	0.0023	27.31	0.28	0.52
	100	1677.72	3.51	0.025	0.0023	29.42	0.31	0.62
LES ₆₄	1	0.26	0.74	0.046	0.0034	48.26	0.23	0.28
	10	2.62	0.74	0.046	0.0034	48.13	0.23	0.28
	50	13.11	0.90	0.044	0.0032	47.54	0.25	0.30
	100	26.21	1.03	0.042	0.0031	47.60	0.27	0.30

Table 1: Variables of the simulations one turnover time after injection for two particle-laden simulations, PP-DNS and PP – LES₆₄.

Figs. 6 and 7 can be interpreted using the turbulent kinetic energy budget introduced earlier. The PP-case without clustering shows a lower dissipation rate (normalized with the referential dissipation rate $\varepsilon_{\text{ref}} = \frac{u_0^3}{L}$) than the sP-case. Both highly-clustered cases show a higher rate over the monitored period of time, which is an unphysical behavior. The coupling rate is negative the whole time for the PP-cases with lower λ_c and positive for the higher-clustered cases. The variables of the DNS and LES₆₄ at $t^* \approx 1$ can be found in Tab.1. Being very similar in the time shortly after the injection, the flow statistics diverge for different λ_c in case of the DNS rapidly. For a high number of CPPs, the simulations drift away from the reference, leading even to unphysical behavior for $\lambda_c \gg 50$. In difference to that, the LES shows less impact to change in CPPs.

In Fig. 8 the kinetic energy of the particles is displayed. For increasing λ_c , the kinetic energy of the particles becomes smaller. This behavior leads to the assumption that the clustering produces the behavior of heavy particles as the results fit to the findings of Schneiders [10].

Fig. 9 can be used to point out the difference in susceptibility for this method. It is evident that a correlation between inaccuracy of the simulations and the refinement level of the grid exists. For the same ratio of physical point particles to CPPs the results show different behavior depending on the grid refinement level. The unclustered PP-case is included as reference. It is therefore less critical to cluster particles in lower-resolution grids, although the results are not nearly as accurate as for the unclustered simulations. A correlation between the fraction of masses of one particle cluster to one cell can be observed in Tab. 1. It seems to be the case that for increasing mass ratio of one cluster to one cell the simula-

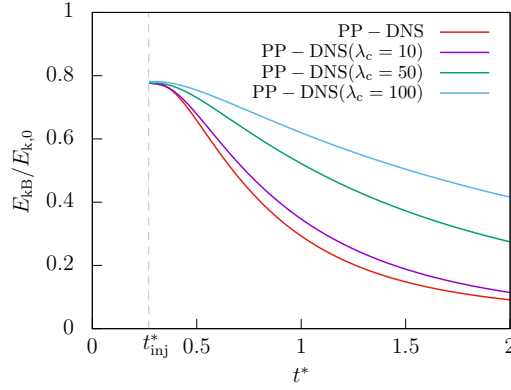


Figure 8: Kinetic energy of the particles E_{kB} normalized by initial turbulent kinetic energy. The PP-case without clustering shows the biggest decay in kinetic energy.

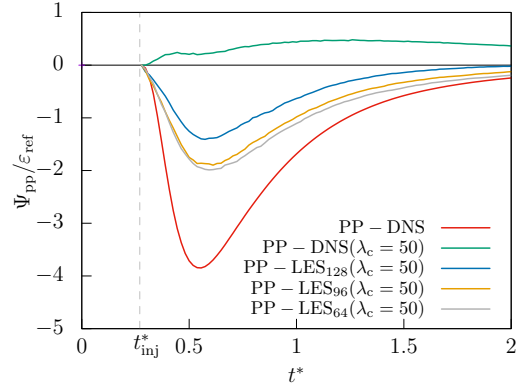


Figure 9: Point-particle coupling rate Ψ_{pp} with constant λ_c for various resolutions. A relation of resolution and accuracy can be observed.

tion results become less accurate. This phenomenon was first described by Maxey and Patel [?], as particle-induced point forces induce a vorticity to the flow at the particle position. Additionally they pointed out that a nonuniform particle distribution, caused by particle inertia or added mass, would have a larger impact on the turbulent kinetic energy of the carrier flow.

The simulation on a 64^3 -grid is therefore less susceptible to altering the CPPs because the cells, and therefore the mass of one cell, are substantially bigger than in the 256^3 -grid for a constant domain size.

5 Conclusion and outlook

In this study, multiple simulations were carried out to evaluate a method for lowering computational effort. The statistics of simulations on multiple resolutions were compared and evaluated. CPPs therefore have been validated, when properly used they could be a useful tool to achieve less computing time.

The DNS showed to be prone for errors created by CPPs. Coupling and dissipation rate were affected very much by them, leading even to unphysical results. In contrast to that the coarser-grid simulations were less prone to CPPs, as multiple comparisons showed. The mass-fraction of one particle-cluster to the fluid content of one cell showed to be an important factor in statistical accuracy. This is because of self-induced disturbances of the particles. These particle clusters seem to behave like heavier particles, as comparisons with results from other literature show.

To enhance understanding and for future improvements of this method, further investigations are needed. There could be simulations to test which mass-fraction delivers sufficient precision while achieving the goal of less computational effort. For this task it is important to define the goal of future simulations of particle-laden isotropic decaying turbulence. For industrial application, a higher number of CPPs could be used, while in scientific work more accurate results are needed.

6 References

- [1] A. Ferrante and S. Elghobashi. On the physical mechanisms of two-way coupling in particle-laden isotropic turbulence. *Phys. Fluids*, 15(2):315–329, 2003.
- [2] A. Prosperetti and G. Tryggvason. *Computational methods for multiphase flow*. Cambridge University Press, 2009.
- [3] A.N. Kolmogorov. The local structure of turbulence in incompressible viscous fluid for very large Reynolds numbers. 30(4):299–303, 1941.
- [4] C. Siewert. *Numerical Analysis of Particle Collisions in Isotropic Turbulence*. PhD thesis, 2014.
- [5] D. Hartmann, M. Meinke and W. Schröder. An adaptive multilevel multi-grid formulation for Cartesian hierarchical grid methods. *Comput. Fluids*, 37(9):1103–1125, 2008.
- [6] D. Hartmann, M. Meinke and W. Schröder. A strictly conservative Cartesian cut-cell method for compressible viscous flows on adaptive grids. *Comput. Methods in Appl. Mech. Eng.*, 200(9):1038–1052, 2011.
- [7] Van Dyke. *An album of fluid motion*. Parabolic Press Stanford, 1982.
- [8] J.R. Fessler, J.D. Kulick and J.K. Eaton. Preferential concentration of heavy particles in a turbulent channel flow. *Phys. Fluids*, 6(11):3742–3749, 1994.
- [9] K. Fröhlich, L. Schneiders, M. Meinke and W. Schröder. Validation of Particle-Laden Large-Eddy Simulation Using HPC Systems. In *Sustained Simulation Performance 2017*, pages 137–149. Springer, 2017.
- [10] L. Schneiders, M. Meinke and W. Schröder. Direct particle–fluid simulation of kolmogorov-length-scale size particles in decaying isotropic turbulence. *J. Fluid Mech.*, 819:188–227, 2017.
- [11] L.F. Richardson. The supply of energy from and to atmospheric eddies. *Proceedings of the Royal Society of London. Series A, Containing Papers of a Mathematical and Physical Character*, 97(686):354–373, 1920.
- [12] M.R. Maxey and J.J. Riley. Equation of motion for a small rigid sphere in a nonuniform flow. *Phys. Fluids*, 26(4):883–889, 1983.
- [13] S. B. Pope. *Turbulent flows*. Cambridge University Press, 2000.

- [14] S. Elghobashi. Particle-laden turbulent flows: direct simulation and closure models. *Appl. Sci. Res.*, 48(3):301–314, 1991.
- [15] S. Elghobashi. On predicting particle-laden turbulent flows. *Appl. Sci. Res.*, 52(4):309–329, 1994.
- [16] S. Hickel. *Implicit turbulence modeling for large-eddy simulation*. PhD thesis, 2008.
- [17] S.A. Orszag. Numerical methods for the simulation of turbulence. *Phys. Fluids*, 12(12):II–250, 1969.
- [18] V. Armenio and V. Fiorotto. The importance of the forces acting on particles in turbulent flows. *Phys. Fluids*, 13(8):2437–2440, 2001.

7 Appendix A

Creating of pictures showing tubular structures

The pictures used in to point out the differences between DNS and LES were generated using ParaView, an open-source-software developed by a joint-venture of Kitware and the Los Alamos National Laboratory. More information about the software can be found at www.paraview.org. To show the tubular structures in a turbulent flow, two filters were used: One was the AIALambda2Criterion1-Filter and the other one was the ISOVolume1-Filter. These filters were then set to visualize the velocity of the flow colored by magnitude. To diversify the different velocity-magnitudes, a rainbow-colorscheme was used.